IEEE Open Journal of
Power Electronics

Received 18 February 2022; accepted 15 March 2022. Date of publication 17 March 2022;
date of current version 7 April 2022. The review of this article was arranged by Associate Editor Rafael Pena-Alzola.

Digital Object Identifier 10.1109/OJPEL.2022.3160416

Real-Time ML-Assisted Hardware-in-the-Loop Electro-Thermal Emulation of LVDC Microgrid on the International Space Station

WEIRAN CHEN (Student Member, IEEE), SONGYANG ZHANG (Student Member, IEEE), AND VENKATA DINAVAHI (Fellow, IEEE)

Department of Electrical and Computer Engineering, University of Alberta, Edmonton, AB T6G 2V4, Canada

CORRESPONDING AUTHOR: WEIRAN CHEN (e-mail: weiran4@ualberta.ca)

This work was supported by the Natural Science and Engineering Research Council of Canada.

ABSTRACT For being the world's largest low voltage direct current (LVDC) microgrid (MG) in space, the power generation and distribution systems aboard the International Space Station (ISS) employ a hierarchical assortment of electric power sources, energy storage, control devices, power electronics, and loads operating cooperatively at multifarious system dispositions and multi-stage configurations. At the early phase of design, for such time-critical systems, the trade-off between reliability and convergence rate of device modeling, varying accuracy requirements of control flows, and especially the implementation for real-time performance have brought new challenges and problems for testing and validation of the MG. One of the solutions presented by this paper is to use the hardware-in-the-loop (HIL) emulation, where the MG is emulated using the field-programmable gate array (FPGA) hardware platform. In parallel with the emulation effort, comprehensive modeling solutions for both large-scale photovoltaic (PV) solar array wings (SAWs) and nonlinear behavior model (NBM) of insulated-gate bipolar transistors (IGBTs) have been utilized based on machine learning (ML) concepts of artificial neural network (ANN) and recurrent neural network (RNN). Both system-level (validated by Matlab/Simulink) and device-level (validated by SaberRD) transient simulations are carried out, and the results exhibit high accuracy and fidelity of the models and significant improvements in execution speed and hardware resource consumption.

INDEX TERMS Artificial neural network (ANN), electromagnetic transients, field-programmable gate arrays (FPGAs), hardware-in-the-loop (HIL), insulated-gate bipolar transistors (IGBTs), International Space Station (ISS), low voltage direct current (LVDC), machine learning (ML), microgrid (MG), photovoltaic, recurrent neural network (RNN), renewable energy, real-time systems, solar array wings (SAWs).

I. INTRODUCTION

Space exploration is receiving growing emphasis in many countries for scientific and commercial applications [1]–[5]. The International Space Station (ISS) is one of the most well-known low earth orbit vehicles, which is a fully functioning, manned, modular, and multinational collaborative space station involving five participating space agencies: Roscosmos (Russia), NASA (United States), JAXA (Japan), ESA (Europe), and CSA (Canada) [6]. The general integrated truss structure (ITS) and low voltage direct current (LVDC) microgrid (MG) of ISS are presented separately in Fig. 1 [7]. Compared with the terrestrial microgrid, the MG on ISS adopted a quintessential multi-bus (160 V to 120 V) LVDC hierarchical centralized control power distribution system, which comprises of the primary power system (PPS), energy storage system (ESS), secondary power system (SPS), and hundreds of nonlinear components such as converters, solar panels, and electrical power consuming equipments (EPCEs). During the architecture layout and requirements analysis phase, it is not reasonably practicable to design the MG as a centralized system and, consequently, due to various reasons such as tight schedule, funding, differences in connectivity, and assembly sequence, each subsystem of the MG will be constructed individually and non-concurrently [7]. Hence, it is

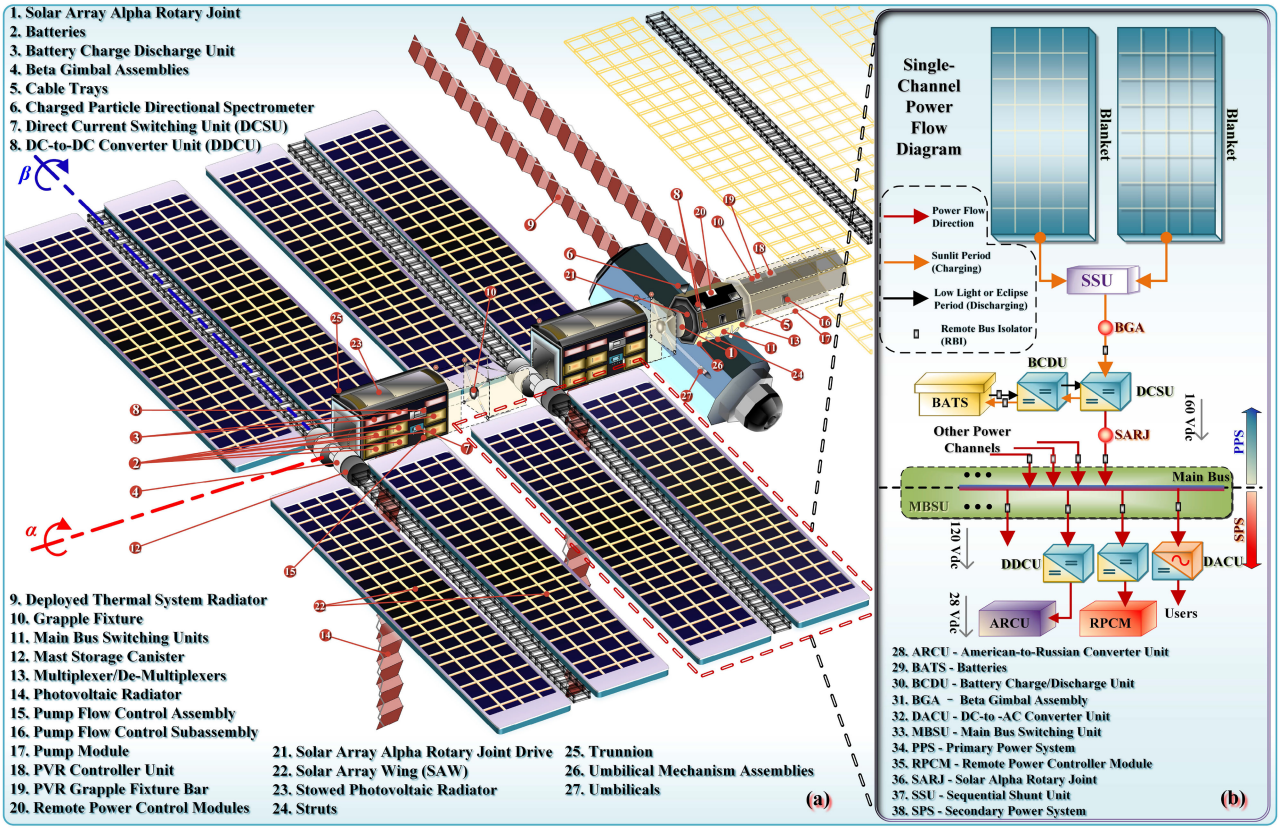

FIGURE 1. Overview of International Space Station (left side): (a) Integrated truss structure; (b) Single-channel power flow.

significant to develop proper simulation models and the real-time hardware-in-the-loop (HIL) emulation of the integrated MG for smooth operations throughout the ISS's on-orbit life span [8].

Significant amount of projects and extensive research related to real-time HIL emulation of the MG has been published in the literature, which can be broadly categorized into three types: 1) design and modeling for partial component, topology or subsystem of MG [9]–[11]; 2) analysis of cosmopolitan experiment modules [12], [13]; 3) studies about the integrated MG [14]–[16]. The development of solar array wings (SAWs), PV power modules (PVMs), and energy storage system are described, highlighting the performance objectives, design description, technical difficulties, test criteria, and results in [9], [10]. With regard to the SPS, a multi-output high efficiency dc/dc power distribution converter [11] and international segments [12], [13] were proposed. For the integrated MG real-time simulation, modeling and testing spacecraft power system based on virtual test bed (VTB) [14], [15] and the Automated State Model Generator (ASMG) based real-time simulator [16] have been established to provide long-term support to the ISS.

Nevertheless, acceleration of computation and reducing resource consumption of the real-time HIL emulator still remains a major challenge. Traditional electromagnetic transient (EMT) simulation tools utilize the nodal, state-space, numerical integration, and piece-wise linear solution methods to solve differential equations in conventional general-purpose compute units such as sequential CPUs. As for the emulation of MG in ISS, because of the nonlinear transcendental $i - v$ relationship of solar cells and nanosecond level execution delay of IGBTs, their computational load significantly aggravates the burden of emulators, and therefore some investigations have been proposed to address these issues [17]–[19]. Furthermore, the performance of emulators is limited by the sophistication degree of models. In order to obtain precise test results as well as feasible real-time capabilities simultaneously, as highlighted above, there is an urgent need to propose more effective modeling methods for ISS emulator bottlenecks, i.e., thousands of solar cells in SAWs and device-level switching devices in ISS MG.

In this scenario, in order to meet the computation ability and memory requirements of real-time systems, the research needs to expand from both algorithm optimization and hardware aspects. For the former, an emerging equivalent prediction fitting approach based on machine learning (ML) and neural networks (NNs) represents a novel way of circuit transient solution, which has been applied in power electronic applications [20], [21]. After learning from given datasets, the NNs produce the Pareto fronts and select the optimal designs, which means the explicit physical significance is only contained inside the input and output variables but not NN itself [22]. In the latter case, as opposed to CPUs that adopt fixed computing architecture, field-programmable

gate arrays (FPGAs) provide an intrinsic parallelism without predefined hardware architecture causing them to be the ideal real-time emulation hardware acceleration platform for the parallelization of NNs [20]. Furthermore, FPGAs have been extensively used for real-time HIL emulation of AC/DC power systems [23].

In this paper, the LVDC MG model with PPS and SPS is established in off-line simulation tools Matlab/Simulink (system-level) and SaberRD (device-level), which offer numerous training datasets under various conditions for training the NNs. For parallelism and optimization, the repetitive and resource-consuming SAWs in PPS and the device-level soft-switching LLC converter in SPS are replaced by artificial neural networks (ANNs) and ANN-recurrent neural network (RNN) hybrid models, respectively. Ultimately, the real-time ML-assisted HIL LVDC MG emulator is implemented on the Xilinx Virtex UltraScale+ FPGA VCU118 board. The results are analyzed and compared with those obtained from traditional EMT-based models. The remainder of this paper is organized as follows: Section II introduces the EMT-based LVDC MG model. In Section III, the basics of NNs and the ML-based modeling method for both system-level and device-level transient emulation are presented. Section IV illustrates hardware implementation of the ISS MG emulator. Results and comparisons are shown in Section V, and finally Section VI gives the conclusion of the work.

II. ISS LVDC MG CONFIGURATION AND MODELING

Electrical power is the lifeblood of ISS, literally, enabling various systems normal operation and to allow astronauts to reside and conduct research. The LVDC MG primarily features eight substantially independent power channels, two of which form one PVM, coupling via converters to transfer power according to requirements and system capacity, as shown in Fig. 1(a) and (b). Each power channel consists of one SAW (containing two foldable solar blankets) and other electric devices to generate, store, and distribute power as an individual source. It is noteworthy that the Russian segment [24] utilizes a separate power supply system, which is not a major part of ISS and has been omitted in this work but can be incorporated in the future. Only the interconnection between US-built 120 V portion and Russian-built 28 V portion is considered, as indicated in Fig. 1(b). The detailed model of the MG is discussed in this section.

A. PRIMARY POWER SYSTEM

The PPS (Fig. 1(b)) is a channelized portion of the MG that operates at a high voltage, stores power during insolation, and supplies electricity for the eclipse. Normally, the SAW provides 160 V during insolation, whereas the batteries provide 151 V during solar eclipse, resulting in the PPS operating voltage range 155 ± 22 V. Under normal conditions, each SAW approximately delivers 31 kW of nominal power while each PVM produces 75 kW of continuous power. The subsystems of PPS are described as follows.

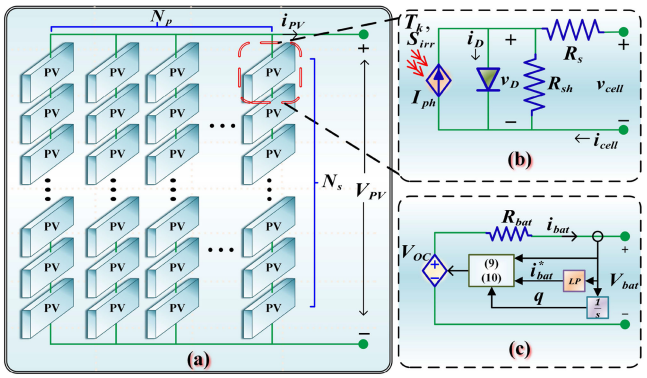

FIGURE 2. SAW equivalent circuit: (a) Solar cell equivalent circuit; (b) $N_p \times N_s$ cells SAW; (c) Shepherd's battery model [28].

1) SOLAR ARRAY WING

Publications that concentrate on solar cell modeling generally adopt transcendental equations to describe the mathematical relationship between cells open-circuit voltage and short-circuit current [18]. Fig. 2(b) gives the single-diode model (SDM) of one basic solar cell unit, whose cell-output current i_{cell} is derived as below:

$$i_{cell}(t) = I_{ph} - I_s \cdot \left(e^{\frac{v_{cell}(t)+i_{cell}(t)\cdot R_s}{V_T}} - 1 \right) - \frac{(v_{cell}(t) + i_{cell}(t) \cdot R_s)}{R_{sh}}, \tag{1}$$

where I_s is the saturation current of the diode, V_T is the thermal voltage, v_{cell} is the voltage across the solar cell electrical ports, R_s is the cell series resistance, R_{sh} is the cell shunt resistance, and solar-induced current I_{ph} features a foreseeable behavior throughout a certain range of operating temperature T_k and light intensities S_{irr}. For multiple series-parallel connection solar cells, Fig. 2(a) illustrates a SAW containing $N_p \times N_s$ cells, which can be deduced as (2) with a similar form to (1) as lumped model of SAW:

$$i_{PV}(t) = N_p I_{ph} - N_p I_s \cdot \left(e^{\frac{V_{PV}(t)+N_s N_p^{-1} R_s i_{PV}(t)}{N_s V_T}} - 1 \right) - \frac{\left(N_p N_s^{-1} \cdot V_{PV}(t) + i_{PV}(t) \cdot R_s\right)}{R_{sh}}, \tag{2}$$

where i_{PV} and V_{PV} are the output current and the voltage across the SAW electrical ports, respectively. Obviously, (1) shows that the expression for i_{cell} is an implicit function containing the transcendental equation, which has contributed to i_{cell} cannot be expressed explicitly using only the elementary function and v_{cell}. For transient simulation, the Lambert W-function and numerical integration such as the Trapezoidal Rule are usually used to obtain the explicit solution and the numerical solution of i_{cell}, respectively [25]. However, these approaches have the drawback of considering the effect of environmental factors, such as light intensity and temperature, on each solar cell of SAW as consistent. Each SAW consists

of 32,800 K6700B Wrapthru solar cells for sufficient power supply during insolation [26], [27]. For such numerous cells based SAW, considering the computational capability and resource consumption of the simulator carrier, it is impractical to treat each solar cell individually. There is a significantly greater temperature difference in the space environment than the terrestrial PV microgrid. Under different conditions such as the sunlit, the eclipse, and the shadows caused by the shading of ISS equipment can cause a severe non-uniform temperature distribution, and traditional EMT computational models fail to reflect such characteristics. Accordingly, the ANN-based SAW modeling method, which will be introduced in detail in Section III, is applied to solve the aforementioned demerits.

2) BATTERY

The ISS requires the introduction of ESS to provide stable control, power quality improvement, and uninterrupted power supply for the whole system. Fig. 2(c) shows a circuit diagram of the modified Shepherd's battery model [28], where R_{bat} is the internal resistance, V_{OC} is the open circuit voltage, i_{bat} is the battery output current, i^*_{bat} is the battery current filtered by a low-pass (LP), $q = \int i_{bat}\,dt$ is the actual battery charge, and V_{bat} is the battery output voltage. Such circuit network employs distinct equations to describe battery charge-discharge dynamics, and the details vary for different battery types. The charging (3) and discharging equations (4) are listed as follows:

$$V_{bat}(t) = E_0 - R_{bat}\cdot i_{bat}(t) - \frac{KQi^*_{bat}}{q-\frac{Q}{10}} - \frac{KQq}{Q-q} + A\cdot e^{-B\cdot q}, \tag{3}$$

$$V_{bat}(t) = E_0 - R_{bat}\cdot i_{bat}(t) - \frac{KQ\cdot\left(q+i^*_{bat}\right)}{(Q-q)} + A\cdot e^{-B\cdot q}, \tag{4}$$

where E_0 is the battery constant voltage, K is the polarization constant, Q is the battery capacity, while A and B are the amplitude and time constant inverse of exponential zone, respectively. The type of Li-Ion cells for usage in ISS is 134-Amp-hr (Ah) LSE134; 30 cells in series form one Li-Ion battery; One Li-Ion battery and an adapter plate (AP) make up a single Orbital Replacement Unit (ORU), three of which are assigned to per channel [10], [29].

3) SEQUENTIAL SHUNT UNIT

The sequential shunt units (SSUs) allow each solar array to be individually connected or disconnected from the PPS. Considering excess energy in the orbit, if batteries are fully charged, the energy rejection function will be activated that causes SSU to automatically shunt certain solar array current to keep operating voltage stable.

4) PPS POWER DISTRIBUTION

As illustrated in Fig. 3, conforming to the power relations among the solar arrays output power P_{PV}, batteries port power P_b, and PPS output power P_o, PPS is designed to work in three modes: 1) Dual-Output Mode (DOM)–solar arrays power flows to batteries and loads, while extra energy is shunted by SSUs; 2) Dual-Input Mode (DIM)–solar arrays and batteries simultaneously power the load; 3) Single-Input Single-Output Mode (SISOM)–batteries provide energy alone [30]. Based on the above power flow analysis, the three-port power conversion system (TP-PCS), as shown in Fig. 4, could be utilized in PPS. In TP-PCS, P_{in} is the output power of SSU, also can be seen as the summation of all connected SAWs output power at any given moment. To maximize P_{in}, the non-inverting buck-boost converter is carried out in SSUs, where V_{PV}, U_{in} and current i_{PV}, i_{in} are SSU input/output voltage and current, respectively. By adjusting the duty ratio d, the proportionality between the left side equivalent resistance R_{PV} and the right side equivalent resistance R_{in} can be changed. In this case, the operating point is reachable throughout the first-quadrant of the $i_{PV}-V_{PV}$ characteristics, so that the maximum power point (MPP) can be successfully tracked. Once excess energy occurring, i_{in} will be shorted to the ground by SSU to roughly keep bus voltage at the set point. In terms of Battery Charge/Discharge Units (BCDUs), they are designed as bidirectional dc-dc converters that switch batteries charging/discharging mode according to reference voltage U^*_b and the undulation of U_{in}. Both power generation portion and ESS are connected to the Direct Current Switch Unit (DCSU), which is the electrical distribution box for a primary power channel. It routes P_{in} and P_b to downstream Main Bus Switching Units (MBSUs) and Direct-Current to Direct-Current Converter Units (DDCUs). Finally, the PPS output voltage U_o and P_o downstream to the MBSU are monitored and regulated synergistically by bidirectional electromechanical relays, i.e. Remote Bus Isolators (RBIs), SSUs, and DCSUs.

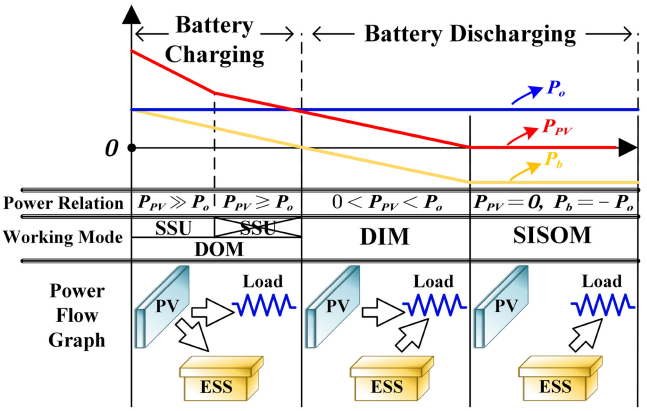

FIGURE 3. Power flow strategy and working mode conversion of PPS.

The control algorithm of TP-PCS is mainly realized by the input voltage regulator (IVR), the battery current regulator (BCR), the battery voltage regulator (BVR), and the output voltage regulator (OVR), where IVR, BCR, and BVR are

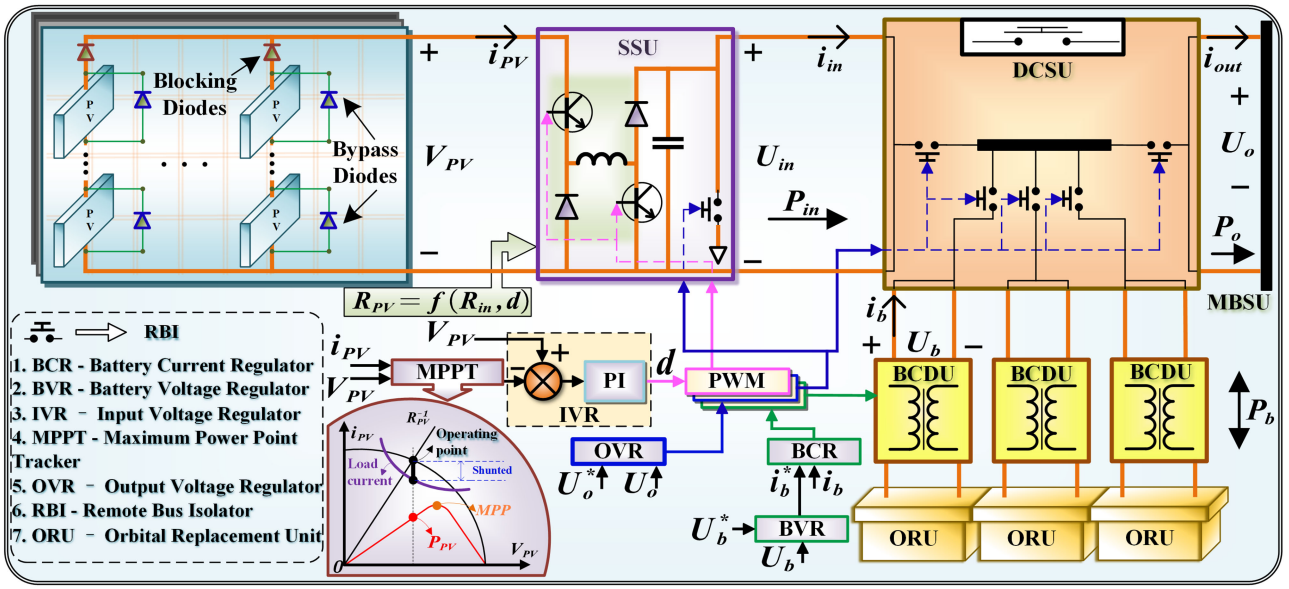

FIGURE 4. Details of the PPS power distribution.

responsible for the control of U_{in}, battery current i_b, and battery voltage U_b, respectively. The reference voltage of IVR is generated from the maximum power point tracking (MPPT) algorithm. Depending on load side needs, the OVR could be replaced by the output current regulator (OCR) or the output power regulator (OPR) for the control of U_o, output current i_{out}, and P_o, respectively.

5) POINTING SYSTEMS

For maximum power production, as can be seen in Fig. 1(a), Solar Alpha Rotary Joints (SARJs) and Beta Gimbal Assemblies (BGAs) are designed to allow SAWs to track the sun as the ISS orbits the Earth. The SARJs and BGAs rotate the PVMs and individual SAWs to provide alpha and beta angle array pointing capability, respectively. In this paper, a dc motor-based sun angle tracking system is utilized to take the place of SARJs and BGAs, which employs motor angular φ position control for tracking sun angle θ. In this case, the SAW output current is described by

$$i_{PV}(t) = I_0 \cos\left(\theta(t) - \varphi(t)\right), \tag{5}$$

where I_0 is the photocurrent with normal sun ($\theta = 0$). The cosine law is not strictly applicable in this situation, especially at low sun angles. The actual power-angle curve of the PV cell is called Kelly cosine, which is useful to assess accurately the power available from sun at low angles during the transfer orbit [31].

B. SECONDARY POWER SYSTEM

The SPS is interfaced with PPS through numerous DDCUs which converter main bus voltage to 120 V and transfer power downstream to international segments and users, which are not represented in detail and replaced by constant power loads. In this section, a device-level, switching frequency

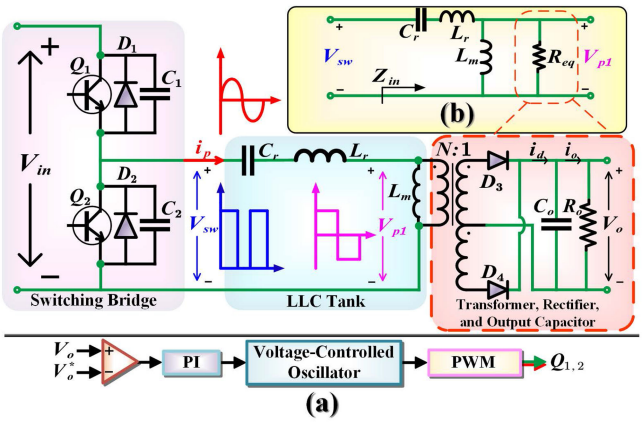

FIGURE 5. (a) Half-bridge LLC converter; (b) Equivalent resonant circuit.

$f_{sw} = 50$ kHz, 5% ripple, 500 W, and 120 V to 28 V LLC converter for American to Russian Converter unit (ARCU) is carried out. Fig. 5(a) shows a half-bridge LLC converter, where the switching bridge generates a square waveform to excite the LLC resonant tank, which will output a resonant sinusoidal current that gets scaled and rectified by the transformer and rectifier circuit, the output capacitor filters the rectified ac current and outputs a dc voltage. To obtain the resonant tank gain, the LLC converter can be simplified as an equivalent resonant circuit, as illustrated in Fig. 5(b), where R_{eq} is the primary side equivalent load. By using the First Harmonic Approximation (FHA) [32], R_{eq} can be derived as

$$R_{eq} = \frac{U_{p1\_rms}}{I_{p1\_rms}} = \frac{8N^2}{\pi^2} R_o, \tag{6}$$

where U_{p1_rms} and I_{p1_rms} are the root-mean-square (RMS) values of fundamental component for primary side voltage

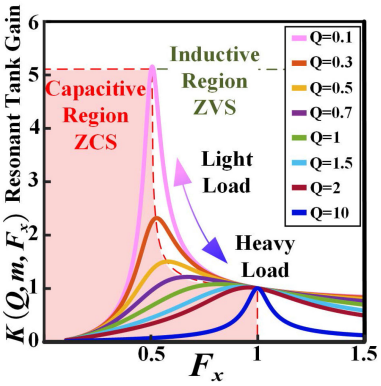

FIGURE 6. Resonant tank gain characteristics of LLC converter.

and current, respectively; N is the transformer ratio, and R_o is the load resistance. Accordingly, the resonant tank gain is the magnitude of its transfer function given as:

$$H(j\omega) = \left|\frac{V_{p1}(j\omega)}{V_{sw}(j\omega)}\right| = \left|\frac{R_{eq}\|j\omega L_m}{Z_{in}(j\omega)}\right| = \left|\frac{R_{eq}\|j\omega L_m}{j\omega L_r + \frac{1}{j\omega C_r} + R_{eq}\|j\omega L_m}\right|, \quad (7)$$

where V_{p1} is the primary side voltage, V_{sw} is the bridge output voltage, C_r is the resonant capacitor, and L_r and L_m are the resonant inductor and transformer magnetizing inductance, respectively. After simplifying and normalizing (7), finally, the resonant tank gain K can be deduced as:

$$K(Q,m,F_x) = \frac{F_x^2(m-1)}{\sqrt{\left(m\cdot F_x^2-1\right)^2 + F_x^2\cdot\left(F_x^2-1\right)^2\cdot(m-1)^2\cdot Q^2}}, \quad (8)$$

where $Q = \frac{\sqrt{L_r/C_r}}{R_{eq}}$ is the quality factor, $F_x = \frac{f_{sw}}{f_r}$ is the normalized switching frequency, $f_r = \frac{1}{2\pi\sqrt{L_r\cdot C_r}}$ is the resonant frequency, and $m = \frac{L_r+L_m}{L_r}$ is the ratio of total primary inductance to resonant inductance. According to (8), all K curves with normalized switching frequency for different values of Q and any single value of m can be plotted, as shown in Fig. 6. It can be seen that low Q curves belong to lighter load operation while higher Q curves represent heavier loads. More importantly, all gain curves have peaks which define the boundary between the inductive and capacitive impedance of the resonant tank. The objective of defining both regions is due to the fact that Zero-Voltage Switching (ZVS) turn-on of primary side IGBTs is only achieved in the inductive region. When IGBT Q_1 is turn-off, parasitic capacitance C_1 charges and the resonant current discharges C_2 voltage to 0 V, creating the conditions for the ZVS of Q_2. Also, the ZVS turn-off condition can be obtained since C_1 and C_2 limit the rising rate of voltage. In terms of secondary side rectifier diodes Zero-Current Switching (ZCS) turn-off, in order to realize ZVS and ZCS at the same time, the LLC converter needs to be operated in the below resonant frequency condition, which means the switching frequency f_s must satisfy $\frac{1}{2\pi\sqrt{(L_r+L_m)C_r}} < f_s < f_r$. In this case, the secondary side rectifier diode current i_d is intermittent, which causes diodes D_3 and D_4 turn-off at a zero current operation. Based on the Infineon design guide [33], after iterations of the design based on the realization of ZVS, ZCS, and required input voltage and load current ranges, $m = 4$ and $f_r = 55$ kHz are chosen. In terms of switches and diodes device selection, the Infineon IHW30N135R5 insulated gate bipolar transistors (IGBTs) and ultrafast soft recovery rectifier diode APT2X101D120 J are selected for $Q_{1,2}$ and $D_{3,4}$, respectively [34], [35]. The entire device-level simulation is built at SaberRD to provide the preliminary database for training the ANN-RNN hybrid model.

III. ML-ASSISTED MODELING METHOD

Although ANNs or RNNs are highly applied in image captioning, natural language processing, and machine translation, such promising ML-based solutions have not yet been promoted widely in the real-time emulation of power systems. This section presents fundamental mathematical principles of ANN and RNN, as well as the merits and demerits of each. In addition, the ANN-based modeling method for SAWs (system-level) and ANN-RNN hybrid modeling method for LLC soft-switching converter (device-level) are discussed in detail.

A. MATHEMATICS OF ANN AND RNN

The neural network is a generic term for a broad category of algorithms based on the concept of machine learning, such as artificial neural network (ANN), convolutional neural network (CNN), recurrent neural network (RNN), long short-term memory (LSTM), gated recurrent unit (GRU), etc. For most cases of power system applications, ANNs based on supervised learning and RNNs with internal memories are widely utilized for numerical prediction, classification, fault detection, and control optimization. Accordingly, in the field of real-time simulation, the characteristics of NNs numerical prediction can be used to derive outputs that conform to the physical laws of power electronics by training from structured data to achieve the purpose of replacing the traditional EMT model [36].

Fig. 7(a) exhibits a typical single layer perceptron ANN, where all inputs, artificial neurons, and outputs are fully connected and layered. Inside every neuron, as shown in Fig. 7(c), the input variables x_i are scaled by the weights w_i, summed with the bias b, and finally processed by the activation function f (Linear, ReLU, or Sigmoid) to obtain the output y of a single neuron. According to whether the system is linear or not, activation functions vary from sigmoid to rectified linear units [22]. Assuming that the layers number of the ANN is k, the number of nodes in the k_{th} layer is m_k, and f^k is

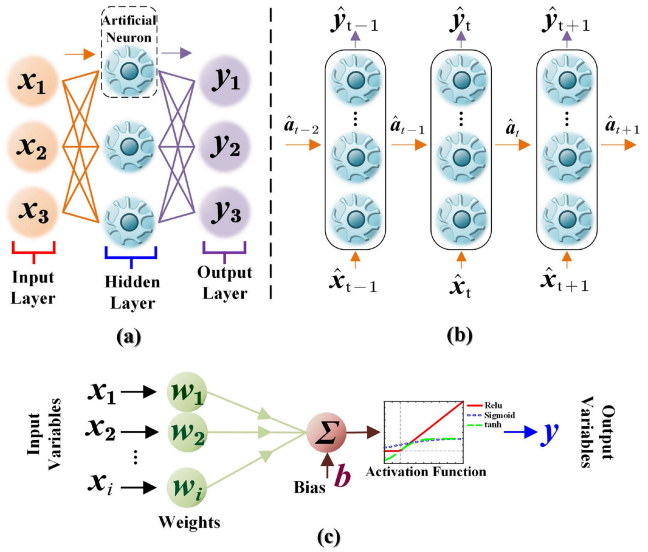

FIGURE 7. (a) Structure of an ANN with three inputs, three outputs, and a hidden layer; (b) forward propagation structure of RNN; (c) internal structure of an artificial neuron.

the activation function of k_{th} layer, then the output vector of the k_{th} layer yields $Y^k = [y_1^k, y_2^k, \ldots, y_{m_k}^k]^T$; the weights are denoted as $W^k \in \mathbb{R}^{m_k \times m_{k-1}}$; and the bias is $b^k \in \mathbb{R}^{m_k}$. Hence, the output $node_i^k$ of the i_{th} node, the output vector net^k of all nodes, and the final output vector Y^k in the k_{th} layer (except the input layer) are listed as follows:

$$node_i^k = \sum_{j=1}^{m_{k-1}} W_{i,j}^k Y_j^{k-1} + b_i^k \, (1 \leqslant i \leqslant m_k), \tag{9}$$

$$net^k = \begin{cases} W^k Y^{k-1} + b^k \\ \left[node_1^k, node_2^k, \ldots, node_{m_k}^k\right]^T \end{cases}, \tag{10}$$

$$Y^k = f^k\left(net^k\right) = \left[Y_1^k, Y_2^k, \ldots, Y_{m_k}^k\right]^T. \tag{11}$$

Eventually, after iterative training and error correction, one ANN with appropriate W^k, b^k, f^k, and the number of layers k can be obtained to predict outputs of physical-based models within a certain error tolerance for given inputs.

The structure of a typical forward propagation RNN is similar to that of a fully-connected ANN. Still, the difference is that the inputs and outputs of the hidden layer of the RNN have an additional weight matrix $\hat{a}$, as shown in the Fig. 7(b). As can be seen from the Fig. 7(b), the output $\hat{y}_t$ of the RNN at t time is influenced not only by the input $\hat{x}_t$, but also by the weight matrix $\hat{a}_{t-1}$ of the output at $t-1$ time. In addition, the updated weight matrix $\hat{a}_t$ is output and fed into the RNN at $t+1$ time. Finally, similar to the mathematical expressions of ANN, with the additional consideration of $\hat{a}$, the mathematical description of RNN can be expressed as:

$$\hat{a}_t = g\left(W_a \hat{a}_{t-1} + W_x \hat{x}_t + b_a\right), \tag{12}$$

$$\hat{y}_t = f\left(W_y \hat{a}_t + b_y\right), \tag{13}$$

TABLE 1 Comparison Between Features of ANN and RNN

Feature	ANN	RNN
Type of data	Tabular data, Text data	Sequence data
Parameter sharing	No	Yes
Recurrent connections	No	Yes
Long-term prediction	No	Yes
Main advantages	Less design difficulty; massive parallelism; faster execution.	Higher accuracy; fewer parameters; less resource consumption.

where W_a and W_x are the weights of $\hat{a}_{t-1}$ and $\hat{x}_t$, respectively, b_a and b_y are the biases of $\hat{a}_t$ and y, respectively, and g and f are the corresponding activation functions, respectively. At the initial moment, $\hat{a}_0$ is specified as a $\vec{0}$ vector. Since $\hat{a}$ is utilized recurrently, the current outputs $\hat{y}_t$ of the RNN network depend not only on the current inputs $\hat{x}_t$, but also on the previous inputs $\hat{x}_{t-1}$. RNNs are marked by this characteristic, making them mnemonic and more suitable for processing time-sequenced data.

B. COMPARISON BETWEEN ANN AND RNN FEATURES

As discussed above, the differences between ANN and RNN can be summarised as follows. Firstly, ANN is a fully connected structure, which is relatively simple and can theoretically fit any linear or non-linear functions by adjusting the number of corresponding neurons and hidden layers. RNN, on the other hand, features relatively complex recurrently connected structures. Because of this, RNN is able to capture the sequential information that appears in the data, while improving the utilisation of the parameters, and reducing the amount of model parameters. Under the same external conditions (same number of hidden layers, training data, and optimisation strategy), the accuracy of RNNs is higher than that of ANNs. However, the special structure of RNN makes it necessary to compute serially to a certain extent, which carries out a higher computational latency compared to ANN. As a result, when choosing the proper neural networks, it is necessary to make a trade-off between computational speed and accuracy. The comparison of features between ANN and RNN is listed in Table 1.

As for the application of electrical power system transient simulation, based on (9)–(13), ANN and RNN are able to fit mathematical models of complex non-linear power electronic components using only matrix addition and multiplication without involving division and matrix inversion. This provides a new possible option for the next generation of EMT solvers. In addition, the structure of the neural network is well suited to parallel computation, which in turn will greatly speed up the solution to the point where real-time simulation is required.

C. ANN-BASED SAW MODEL

As previously discussed in Section I and Section II, the main challenge for detailed system-level SAW simulations is the huge computational burden and poor real-time performance imposed on the emulator. In addition, light intensities and

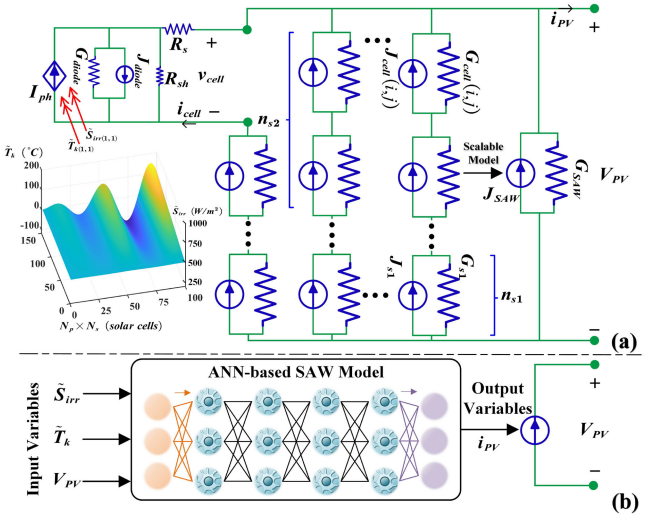

FIGURE 8. (a) Scalable SAW model; (b) ANN-based SAW model.

temperature input to the solar power arrays are typical of tabular data. Therefore, the ANN with faster execution speed is chosen. The detailed ANN-based SAW model design process is presented as follows.

1) DATASET PREPARATION

As presented in Section II, the lumped SAW model with $N_p \times N_s$ cells could be accessed from Matlab/Simulink's Simscape/Electrical library and simulated to obtain the desired datasets. However, this lumped model fails to reflect the uniqueness of each solar cell, and the workload is too heavy to simulate numerous solar cells individually. In this case, it is necessary to build a scalable SAW model in order to collect the simulation results of an arbitrary scale SAW as datasets. As shown in Fig. 2(b) and Fig. 8(a), after seeking partial derivative of the diode voltage $v_D(t)$, the equivalent equations for the conductance G_{diode} and equivalent current source J_{diode} of the nonlinear diode are arrived, given by

$$G_{diode} = \frac{\partial i_D(t)}{\partial v_D(t)} = \frac{I_s}{V_T} \cdot e^{\frac{v_D(t)}{V_T}}, \tag{14}$$

$$J_{diode} = i_D(t) - G_{diode} \cdot v_D(t), \tag{15}$$

where i_D is the diode current. As a result, after obtaining all the required discrete equations, replacing the electronic components with current sources and resistors or conductors, the two-node Norton equivalent circuit of a single solar cell is derived:

$$J_{cell} = \frac{I_{ph} - J_{diode}}{G_{diode}R_s + R_sR_{sh}^{-1} + 1}, \tag{16}$$

$$G_{cell} = \frac{G_{diode} + R_{sh}^{-1}}{G_{diode}R_s + R_sR_{sh}^{-1} + 1}. \tag{17}$$

After that, the SAW is considered to consist of N_p parallel strings and $n_{s1} + n_{s2}$ series cells with flexible number n_{s1} and n_{s2}, where $N_s = n_{s1} + n_{s2}$. It is worth noting that where the input temperature and light intensities of solar cells on some certain parallel strings do not vary much, n_{s1} can be set as the length of the lumped PV model to reduce the computational burden. The lumped PV model of n_{s1} length is expressed below:

$$G_{s1} = \left(\sum_{j=1}^{n_{s1}} G_{cell}^{-1}(j) \right)^{-1}, \tag{18}$$

$$J_{s1} = \sum_{j=1}^{n_{s1}} \left(J_{cell}(j) G_{cell}^{-1}(j) \right) \cdot G_{s1}, \tag{19}$$

Finally, the overall detailed scalable SAW model can be derived as follows:

$$G_{SAW} = \sum_{i=1}^{N_P} \left(G_{s1}^{-1} + \sum_{j=n_{s1}+1}^{n_{s2}} G_{cell}^{-1}(i,j) \right)^{-1}, \tag{20}$$

$$J_{SAW} = \sum_{i=1}^{N_p} \left(\begin{pmatrix} J_{s1}G_{s1}^{-1} \\ + \sum_{j=n_{s1}+1}^{n_{s2}} J_{cell}(i,j) G_{cell}^{-1}(i,j) \end{pmatrix} \cdot \left(G_{s1}^{-1} + \sum_{j=n_{s1}+1}^{n_{s2}} G_{cell}^{-1}(i,j) \right)^{-1} \right), \tag{21}$$

where i and j denote the i_{th} string and j_{th} series cell, respectively. The choice of n_{s1} and n_{s2} depends primarily on the accuracy required for the simulation results. Based on this detailed scalable SAW model, the ideal accuracy i_{PV} output datasets can be collected under various simulation conditions. As for the collection of V_{PV} datasets, they can be simply measured with a voltage sensor connected in parallel to the load side of the SAW model, or calculated by i_{PV}. Finally, the operating temperature $\tilde{T}_k$ and light intensities $\tilde{S}_{irr}$ are determined by different environmental conditons. Fig. 8(a) shows an example of the sine increasing distribution of $\tilde{T}_k$ and $\tilde{S}_{irr}$ over a 150×100 cells SAW, where $\tilde{T}_k \in (-120, 160)^{\circ}$C and $\tilde{S}_{irr} \in (0, 1000)\ W/m^2$.

2) INPUT/OUTPUT VARIABLES

It can be seen from Fig. 8(b), the ANN-based SAW can be considered as a controlled current source with inputs of temperature $\tilde{T}_k$, light intensities $\tilde{S}_{irr}$, and load side voltage V_{PV}. The output variable i_{PV} is checked against the test datasets provided by the $i_{PV} - V_{PV}$ characteristics obtained from Matlab/Simulink simulations and the scalable SAW model. Afterwards, it is crucial to normalize all datasets to $(-1, 1)$ by min-max normalization as pre-processing in order to improve training efficiency and ANNs performance.

D. ANN-RNN HYBRID BASED LLC CONVERTER MODEL

In order to model the device-level soft-switching LLC converter and observe the switching transients, an ANN-RNN hybrid IGBT model is proposed, as represented in Fig. 9. One RNN and one ANN are responsible for the system-level steady-state simulation and device-level transient simulation of the switches, respectively. The reason for not using single

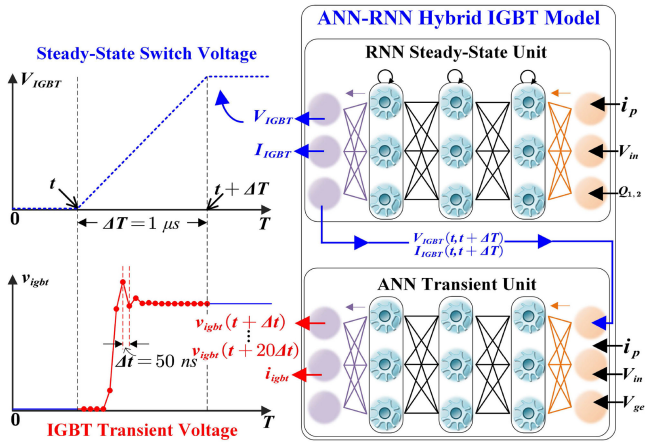

FIGURE 9. ANN-RNN hybrid IGBT model.

ANN or RNN to simulate the switches is that the device-level mathematical relationships within the switches are relatively sophisticated, which leads to an increase in the complexity of the network structure and fails to meet the real-time simulation requirements. Besides, it is difficult to train because the switching transient waveform of IGBT is very different from its steady-state behavior but occupies a small proportion of the entire cycle. In this case, the switch model is divided into two areas, each area can be represented by a functional unit and each unit only focuses on specific applications and leverage the strengths of a separate structure.

As can be seen in Fig. 9, for steady-state simulation, the RNN steady state unit is chosen for its higher accuracy and less resource consumption. Take the IGBT turn-off transient as an example, the RNN unit outputs IGBT steady-state voltage V_{IGBT} and current I_{IGBT} in a large time step $\Delta T = 1\,\mu s$. The steady-state outputs at time t and $t + \Delta T$ are taken as inputs to another functional unit, which is the ANN transient unit. The ANN is chosen for its massive parallelism and faster execution delays meeting the nanosecond level requirements of IGBT transient simulations. The ANN transient unit will recalculate the transient waveform for the time ΔT interval in small steps of $50\,ns$ after receiving the steady state inputs and outputs 20 points simultaneously to complete the process of IGBT device-level transient simulation.

1) DATASET PREPARATION

Unlike the scalable SAW model, the device-level LLC converter could be easily built by the components provided in SaberRD. The converter is then simulated to generate the LLC primary side current i_P, converter input voltage V_{in}, the PWM signal $Q_{1,2}$, gate-emitter voltage V_{ge} datasets, and steady state IGBT voltage V_{IGBT}, IGBT current I_{IGBT}, transient IGBT voltage v_{igbt}, and IGBT current i_{igbt} datasets.

2) INPUT/OUTPUT VARIABLES

The input variables of the ANN-RNN hybrid IGBT model are i_P, V_{in}, $Q_{1,2}$, and V_{ge}, and the output variables are V_{IGBT}, I_{IGBT}, v_{igbt}, and i_{igbt}. It is worth noting that outputs V_{IGBT} and I_{IGBT} are also inputs to the ANN transient unit within the model. All input and output variables are processed similarly as the ANN-based SAW model, i.e., all variables are normalized to $(-1, 1)$ using min-max normalization. Finally, the ANN-RNN hybrid IGBT models are connected to the LLC converter in the form of a controlled voltage source.

E. TRAINING AND ERROR CORRECTION

The proposed ANN or ANN-RNN hybrid model is based upon supervised learning, which is a typical machine learning task of learning a function that maps inputs to outputs based on example input/output pairs and it infers a function from labeled training data consisting of a set of training examples [37]. The input/output pairs are input/output variables of the models mentioned above, such as $\tilde{T}_k$, $\tilde{S}_{irr}$, V_{PV}, and i_{PV}. The labeled datasets, also known as validation datasets or test datasets, are the outputs of traditional EMT models, such as V_{IGBT}, I_{IGBT}, v_{igbt}, and i_{igbt}. The input/output pairs are usually divided into the training set, the validation set, and the test set in the ratio of 6 : 3 : 1 [38]. The training of ANN or ANN-RNN hybrid model (hereinafter referred to as ANN), in simple terms, is the process of tuning parameters, i.e., weights and biases.

For the first iteration, the parameters are randomly initialized. And then, the ANN outputs are compared to the labeled datasets to calculate the error metrics. The mean absolute error (MAE) is chosen as the error criterion, expressed as follows:

$$MAE = \sum_{i}^{n} \frac{|\tilde{y}_i - y_i|}{n}, \tag{22}$$

where $\tilde{y}_i$ is the i_{th} output of ANN, y_i is the i_{th} labeled data, and n is the number of total outputs. Afterward, the gradient of the MAE with respect to the weights is computed. This is achieved by applying, systematically, the chain rule for the derivative and done layer by layer from the outputs to the inputs, i.e., backpropagation (BP) [22]. One of the most popular stochastic gradient descent (SGD) optimization algorithm, Adam algorithm is utilized to minimize the MAE [39], [40]. This process is repeatedly iterated to obtain the ideal optimal weights (the biases are similarly selected).

The selection of activation functions and the layer size are also essential. The $tanh()$ and $ReLU()$ are selected as activation functions since the $sigmoid()$ suffers from vanishing gradient [38]. In terms of the layer size, theoretically, the number of hidden layers is proportional to the accuracy of outputs. However, an excessively deep and complex neural network can cause high resource consumption, long execution delay, and exploding gradient. The hidden layer size in this research is four times larger than the inputs, and the sequence length of the RNN is three. Despite that, the choice of these parameters is elastic and varies according to the complexity of different models.

Once the ANN model and ANN-RNN hybrid model have been well-trained and tested, both the EMT-based LVDC MG in ISS and the ML-assisted MG model are built in C language.

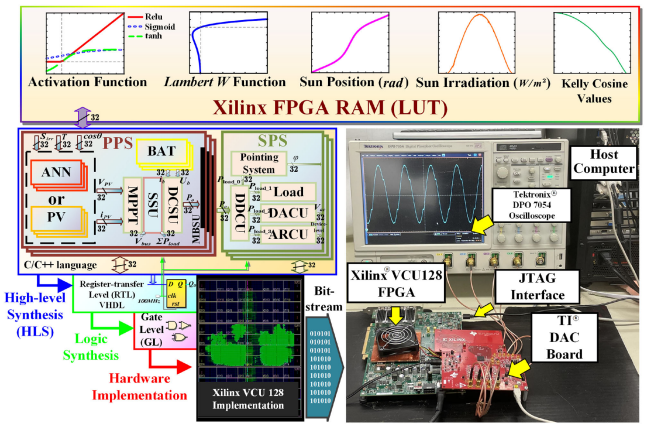

FIGURE 10. Top-level design flow of the real-time emulator, functional block diagram, and hardware platform configuration.

TABLE 2 FPGA Hardware Resource Consumption of MG

Module	Latency	BRAM	DSP	FF	LUT
System-Level MG on VCU128 ($100MHz$)					
One EMT-based PVM	173 T_{clk}	0.74%	14.05%	3.97%	9.07%
One ESS	144 T_{clk}	0.35%	1.60%	0.64%	1.83%
One pointing system	110 T_{clk}	0.30%	4.17%	1.16%	2.66%
One DDCU	99 T_{clk}	0.45%	3.09%	0.97%	2.10%
One DCAC	105 T_{clk}	0.45%	5.11%	1.58%	4.14%
One LLC converter	127 T_{clk}	1.04%	2.66%	0.82%	2.44%
One ANN-based PVM	331 T_{clk}	0.84%	7.65%	2.49%	6.57%
Device-Level MG on VCU128 ($100MHz$)					
One ANN-RNN hybrid IGBT	37 T_{clk}	4.27%	4.43%	0.33%	2.63%

At this point, the preliminaries for the real-time ISS emulator are ready.

IV. FPGA-BASED REAL-TIME HARDWARE EMULATION

The entire real-time emulator of ISS including one PVM, two SAWs, four power channels and SPS was implemented on the Xilin Virtex UltraScale+ XCVU37P (VCU128) FPGA. Fig. 10 shows the top-level design flow of the emulator. All necessary datasets, such as sun position and irradiation by courtesy of the National Aeronautics and Space Administration (NASA) [41]; the LambertW function; the Kelly cosine values [31] and activation functions, can be read from the lookup tables (LUTs). The whole system is built by C language in Xilinx high-level synthesis (HLS) tool, which converts high-level programming language to VHDL or Verilog. After the co-simulation of the register-transfer level (RTL) design and C design is verified, the project is described at gate level (GL) through the logic synthesis (LS) tool for hardware implementation. Finally, the bitstream file is generated and downloaded into the FPGA.

The FPGA is operated at 100 MHz clock frequency and supplies 4,032 random-access memories (BRAMs), 9,024 digital signal processors (DSPs), 2,607,360 flip flops (FFs), 1,303,680 LUTs, and 704 maximum user I/O pins for hardware resource utilization of the emulator, listed as Table 2 and Table 3. Particularly, it can be seen from Table 3 that in the ideal case where $n_{s2} = 0$ and environment conditions

TABLE 3 FPGA Hardware Resource Consumption and Latency Comparison Between EMT-Based PVM and ANN-Based PVM

$n_{s1} : n_{s2}$	Cells No.	Latency	BRAM	DSP	FF	LUT
EMT-based PVM on VCU128 ($100MHz$)						
$1:0$	4,800	73 T_{clk}	0.24%	7.81%	1.56%	6.77%
$1:2^0$	9,600	173 T_{clk}	0.74%	14.05%	3.97%	9.07%
$1:2^1$	14,400	220 T_{clk}	1.14%	17.89%	6.32%	13.39%
$1:2^2$	24,000	368 T_{clk}	0.84%	25.02%	7.16%	15.90%
$1:2^3$	43,200	3721 T_{clk}	0.94%	32.73%	13.56%	25.40%
ANN-based PVM on VCU128 ($100MHz$)						
$1:0$	4,800	294 T_{clk}	0.96%	2.17%	1.22%	3.00%
$1:2^0$	9,600	331 T_{clk}	1.24%	3.17%	1.73%	4.01%
$1:2^1$	14,400	340 T_{clk}	0.84%	7.65%	2.49%	6.57%
$1:2^2$	24,000	348 T_{clk}	0.92%	10.01%	8.03%	8.68%
$1:2^3$	43,200	397 T_{clk}	1.91%	15.16%	11.05%	15.12%

are consistent, the EMT-based lumped SAWs model outperforms the ANN-based SAWs model in terms of resources and latency. However, under varying temperature and light irradiation conditions, as the number of solar cells n_{s2} increasing, the resource consumption and latency of EMT-based model also grow exponentially. Taking (21) as an example, five matrix inversion operations are needed to find just one equivalent current source. The large number of n_{s2} will lead to numerous matrix operations, which will greatly increase the resource consumption and computational latency, resulting in poor real-time performance. On the contrary, the ANN-based models, which feature highly parallelized structure and perform only multiplication and addition operations, are not affected much and still performs well ($< 4\,\mu s$). The real-time performance of the entire emulator is $2\,\mu s$ time-step (ideal case) to $4\,\mu s$ time-step (non-ideal case) at system-level. While for the ANN-RNN hybrid device-level models, each computational iteration performed in the FPGA generates 20 data points spaced at $50\,ns$ intervals to produce the switching transient waveform in a linear interpolation method.

V. REAL-TIME HARDWARE EMULATION RESULTS

In this section, the proposed ANN-based SAWs and ANN-RNN hybrid based LLC converter are validated using the commercial simulation tool Matlab/Simulink and SaberRD under various conditions. The real-time emulation results of LVDC MG model are collected on the Tekronix DPO 7054 Oscilloscope.

A. SIMULATION VALIDATION FOR SAWS

Three independent variables are set for testing the SAWs: 1) light intensities $0 \leqslant S_{irr} \leqslant 1200, W/m^2$; 2) operating temperature $-180 \leqslant T \leqslant 60, ^\circ C$; 3) the number of PV array blocks n_{s2} under nonuniform environmental conditions. Each SAW consists of $n_{s1} + n_{s2}$ arrays and each array contains 4,800 solar cells. Fig. 11(a) shows that I_{PV} generated by one SAW operating at a constant temperature rises as S_{irr} rises, and when eclipse occurs, almost no current is produced, while at full sun, a single SAW can generate up to nearly 240 A short circuit current, which matches the result in [7]. It can be seen that under ideal conditions, both models are highly

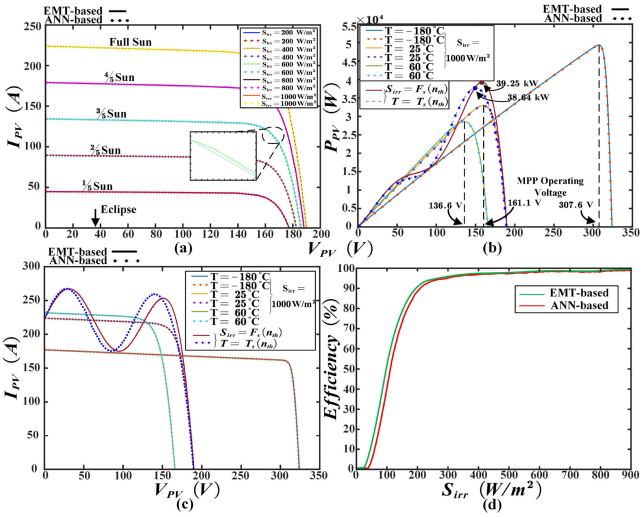

FIGURE 11. (a) Single SAW $I_{PV} - V_{PV}$ characteristics at 25 °C. (b) Single SAW $P_{PV} - V_{PV}$ characteristics at various temperatures and irradiance. (c) Single SAW $I_{PV} - V_{PV}$ characteristics at various temperatures and irradiance. (d) Efficiency comparison for EMT-based and ANN-based SAWs.

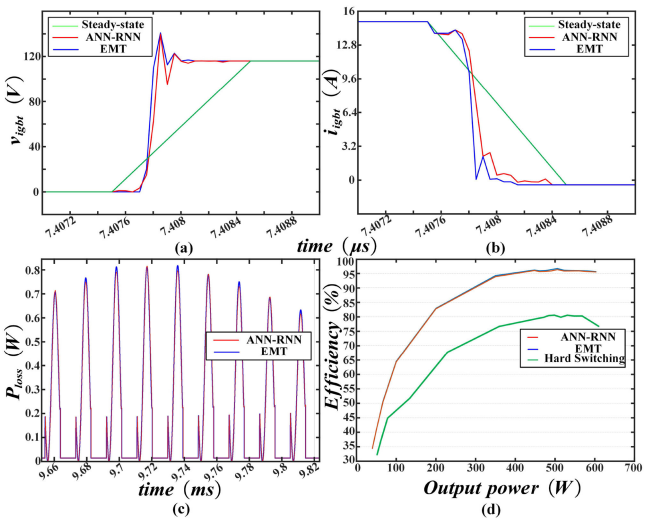

FIGURE 12. (a) Device-level IGBT output voltage. (b) Device-level IGBT output current. (c) IGBT power loss. (d) Efficiency comparison for ANN-RNN hybrid based LLC and EMT-based LLC.

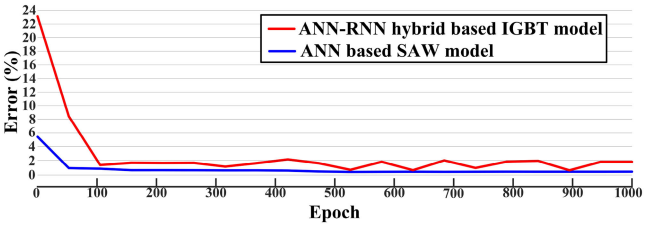

FIGURE 13. Models' error percentage during training processes.

matched. Fig. 11(b) and (c) depict the power and current output versus voltage characteristics at various temperatures and irradiation with maximum gaps of 0.61 kW and 7.14 A, respectively. It shows that the maximum power generated at the lower temperature is higher, which means cold temperatures are better for SAWs for power generation. However, the operating voltage points for each MPP are not the same. Considering the lifetime of PV devices in ISS, 160 V will usually be set as the operating point. Particularly, for nonuniform environmental conditions tests, the equations for temperature ($^{\circ}C$) and irradiation (W/m^2) are designed as follows:

$$\begin{cases} S_{irr} = F_s\left(n_{th}\right) = 800 + 200 \cdot n_{th} \cdot \sin\left(2\pi f\right) \\ T = T_s\left(n_{th}\right) = 25 + 2 \cdot n_{th} \cdot \sin\left(2\pi f\right) \end{cases}, \tag{23}$$

where n_{th} is the nth one n_{s2} array, and $f = 1$ Hz. As proven in Fig. 11(b), there exhibits a gap of 6.2 kW between MPPs for nonuniform conditions and ideal conditions. This difference will be significantly magnified as the number of arrays increases and the complexity of the environmental conditions rises. Fig. 11(d) shows the efficiency of the two SAW models at different light intensities, from which it can be seen that the output efficiency of the SAW is proportional to the light intensities. Meanwhile, the ANN-based models and the EMT-based models produce differences, but the error is still less than 2%, which is acceptable considering the resource optimization and real-time implementation.

B. SIMULATION VALIDATION FOR LLC

In terms of device-level LLC converter, taking the transient of the IGBT turn-off as an example, Fig. 12(a) and (b) illustrate the difference in performance between the ANN-RNN hybrid based and EMT based IGBT models. The results match perfectly in the steady-state phase with only minor differences in the transient phase. As the transient time step is only 50 ns, the differences will not cause significant errors in IGBT power loss calculation. Fig. 12(c) shows the switching losses of the two models, the maximum difference of which does not exceed 0.1 W. Finally, Fig. 12(d) presents the efficiency of two models under different load conditions. Under the rated condition, the efficiencies of the ANN-RNN hybrid based model and the EMT-based model are 96.3% and 96.7% respectively, with errors within the permitted range.

Fig. 13 shows the error ratio of ANN-based SAW model (n_{s1}:$n_{s2} = 1:1$) and ANN-RNN hybrid based IGBT model during the 1000 training epochs. A training epoch is completed when all sampling datasets have been used. The results show that all ANN or ANN-RNN based models utilized in this work feature an error rate of less than 2% after 1000 training epochs.

C. REAL-TIME EMULATION RESULTS OF LVDC MG ON ISS

Fig. 14 exhibits real-time LVDC MG emulation results of system-level ($n_{s1} : n_{s2} = 1:1$) and device-level for ML-assisted model and EMT-based model with prefix *NN* and *EMT*, respectively. In the interest of brevity, the validation results from Matlab/Simulink and SaberRD have been omitted. The ISS real orbiting Earth datasets were normalized from 90 minutes to 20 seconds, and inputs were manually set to jump every 2 seconds during the first 10 seconds,

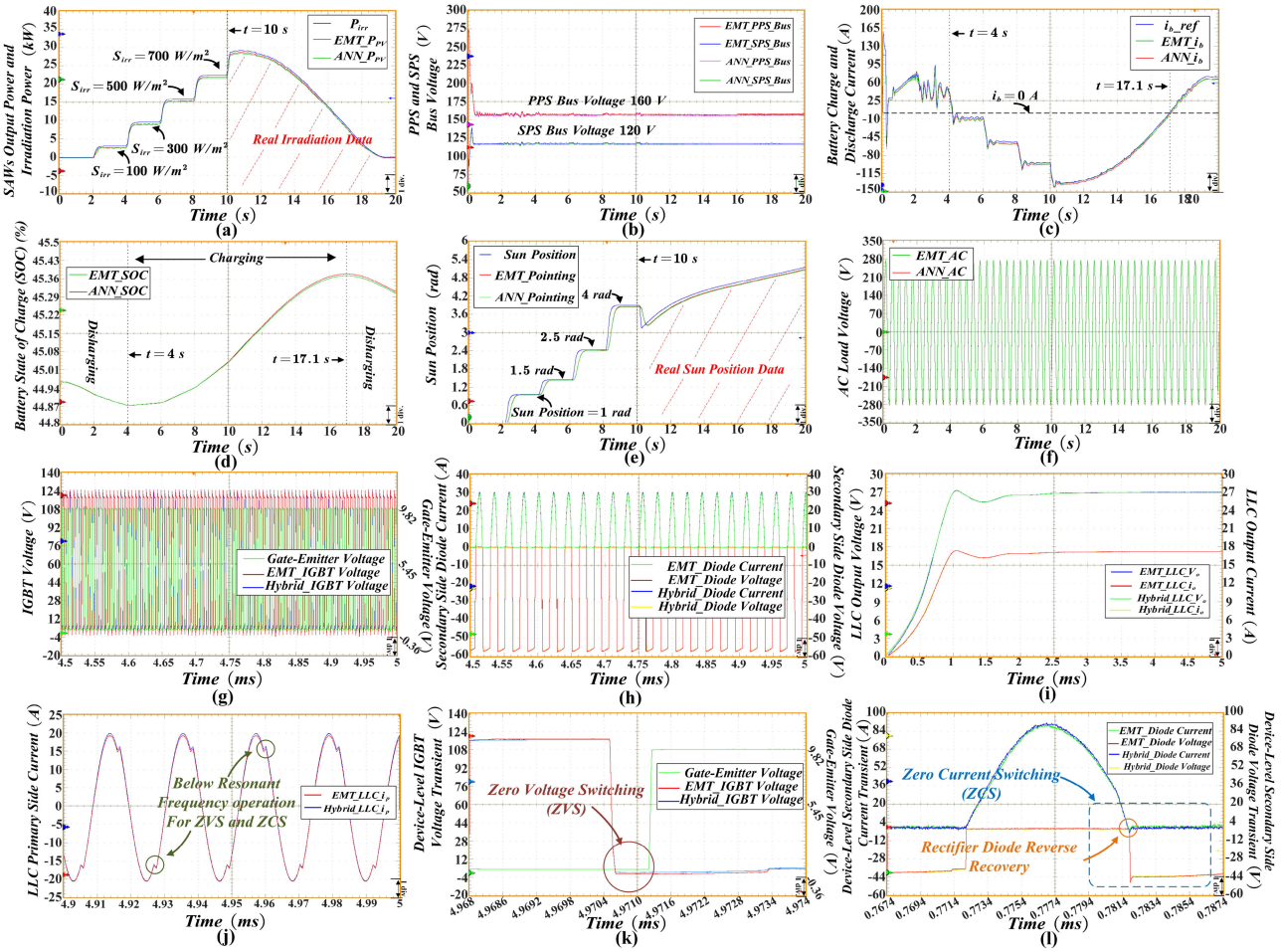

FIGURE 14. System-level real-time emulation results: (a) Light irradiation input power P_{irr} and SAWs output power variables; (b) PPS and SPS bus voltage; (c) Battery reference current i_b_ref, and battery current variables; (d) Battery SOC variables; (e) Sun reference position *Sun_Position*, and pointing system output variables; (f) AC load voltage variables. Device-level LLC converter real-time emulation results: (g) IGBT voltage and gate-emitter voltage; (h) Rectifier diodes current and voltage; (i) LLC converter output voltage and current; (j) LLC primary side current; (k) IGBT ZVS transients; (l) Rectifier diodes ZCS transients. Scale: (a)-(e), (f) x-axis: 2 s/div. (g) (h) x-axis: 0.05 ms/div. (i) x-axis: 0.5 ms/div. (j) x-axis: 0.01 ms/div. (k) 0.6 $\mu s/div$. (l) x-axis: 2 $\mu s/div$.

and then switched to the real datasets (light irradiation range from 0 W/m^2 to 1000 W/m^2 and temperature jumping around 22 °C) at $t = 10$ s, as shown in Fig. 14(a). It can be seen that both models track the MPP P_{irr} well due to the MPPT control. Fig. 14(b) shows the PPS bus voltage (160 V) and the SPS bus voltage (120 V). After the system starts up, there are slight ripples in the bus voltage as the inputs jump, but when the inputs switch to relatively smooth real data, bus voltages are more stable. For ESS, Fig. 14(c) and (d) present the trend of battery current and state of charge (SOC). From $t = 0$ s to $t = 4$ s, due to the weak light irradiation, the battery reference current i_b_ref turns positive, the battery starts to discharge to power the system with SOC decreasing. Between $t = 4$ s and 17.1 s, as the light increasing, i_b_ref turns negative, and the power channel charges batteries while powering the load, and so on repeatedly the battery charge-discharge periodic processes. Fig. 14(e) indicates both pointing systems respond within 1 s and track sun position from 0 rd to 5.3 rd. Fig. 14(f) illustrates a 50 Hz, 5 kW, and 220 V (rms) AC load voltage at SPS load side, from which it can be seen that there is little difference between the output results of the ML-assisted model or EMT-based model at the SPS. For device-level LLC converter simulation, the steady-state voltage and gate-emitter voltage of the primary side IGBTs, and the steady-state voltage and current of the secondary side rectifier diodes are shown in Fig. 14(g) and (h), respectively. Also, Fig. 14(i) exhibits that the LLC converter is able to stabilize and outputs 28 V required by ARCU within 2 ms. The primary side current i_p appears with a plateau for a positive slope, as shown in the Fig. 14(j), which indicates that the converter is operated at below resonant frequency. For ZVS, it can be observed from Fig. 14(k) that the switching voltage is reduced to 0 V in advance when the gate-emitter voltage arrives. In terms of ZCS, i_d is discontinuous causing a zero current at turn-off operation, as illustrated in Fig. 14(l). As can be seen from the figures and discussion above, the ZVS of the primary side IGBTs and the ZCS of the secondary side diodes are realized simultaneously, which greatly improves the converter efficiency compared to the hard switches converter.

VI. CONCLUSION AND FUTURE WORK

This paper proposed a real-time ML-assisted HIL electro-thermal emulation of the LVDC MG on the ISS under nonuniform environment conditions with system-level (2 μs for ideal cases and 4 μs for non-ideal cases) and device-level (50 ns) on the FPGA. The contributions of this work are listed as follows: 1) The ANN-based PV modeling method under varying conditions accelerates the real-time emulation execution time by nearly nine times compared to the EMT-based method while reducing the resource consumption by half; 2) for nonlinear complex electronics modeling such as IGBTs and diodes, the presented ANN-RNN hybrid modeling approach also exhibits reliable real-time performance and high-execution efficiency, which provides a new solution for device-level components modeling; 3) the results demonstrate high reliability with errors less than 2%, which provides another reliable real-time modeling solution for engineers to design and test spacecraft power systems considering complex environmental factors; 4) this work provides and validates the possibility of joint ML and EMT modeling methods, which presents a more flexible simulation option depending on the requirements of projects. In future work, the real-time multi-domain modeling and emulation of spacecraft will be taken into consideration.

REFERENCES

[1] P. A. Jones and B. R. Spence, "Spacecraft solar array technology trends," *IEEE Aerosp. Electron. Syst. Mag.*, vol. 26, no. 8, pp. 17–28, Aug. 2011.

[2] S. J. Edberg, D. L. Evans, J. E. Graf, J. J. Hyon, P. A. Rosen, and D. E. Waliser, "Studying earth in the new millennium: NASA jet propulsion Laboratory's contributions to earth science and applications space agencies," *IEEE Geosci. Remote Sens. Mag.*, vol. 4, no. 1, pp. 26–39, Mar. 2016.

[3] S. Marcuccio, S. Ullo, M. Carminati, and O. Kanoun, "Smaller satellites, larger constellations: Trends and design issues for earth observation systems," *IEEE Aerosp. Electron. Syst. Mag.*, vol. 34, no. 10, pp. 50–59, Oct. 2019.

[4] G. Furano *et al.*, "Towards the use of artificial intelligence on the edge in space systems: Challenges and opportunities," *IEEE Aerosp. Electron. Syst. Mag.*, vol. 35, no. 12, pp. 44–56, Dec. 2020.

[5] A. Shirazi, J. Ceberio, and J. A. Lozano, "Simulation framework for orbit propagation and space trajectory visualization," *IEEE Aerosp. Electron. Syst. Mag.*, vol. 36, no. 8, pp. 4–20, Aug. 2021.

[6] E. Huckins and P. Ahlf, "Space station power requirements and issues," *IEEE Aerosp. Electron. Syst. Mag.*, vol. 9, no. 12, pp. 3–7, Dec. 1994.

[7] E. Gholdston, J. Hartung, and J. Friefeld, "Current status, architecture, and future technologies for the international space station electric power system," *IEEE Aerosp. Electron. Syst. Mag.*, vol. 11, no. 2, pp. 25–30, Feb. 1996.

[8] D. M. Lengyel and J. S. Newman, "International space station lessons learned for space exploration," *NASA Public Lessons Learned System Database*, vol. 39, Sep. 2014, Art. no. 12603.

[9] C. Winslow, "Space station freedom solar array design development," *IEEE Aerosp. Electron. Syst. Mag.*, vol. 8, no. 1, pp. 3–8, Jan. 1993.

[10] E. Schwanbeck and P. Dalton, "International space station Lithium-ion batteries for primary electric power system," in *Proc. Eur. Space Power Conf.*, 2019, Art. no. 1.

[11] F. Belloni, P. G. Maranesi, and M. Riva, "DC/DC converter for the international space station," *IEEE Aerosp. Electron. Syst. Mag.*, vol. 46, no. 2, pp. 623–634, Apr. 2010.

[12] J. de Carufel, E. Martin, and J.-C. Piedbœuf, "Control strategies for hardware-in-the-loop simulation of flexible space robots," *IEE Proc.-D: Control Theory Appl.*, vol. 147, no. 6, pp. 569–579, 2000.

[13] P. Berthe, A. P. Over, M. Picardo, and A. Byers, "Orion European service module (ESM) development, integration and qualification status," in *Proc. AIAA SPACE, Astronaut. Forum, Expo.*, Sep. 2017, Art. no. 5146.

[14] J. R. Lee, B. H. Cho, S. J. Kim, and F. C. Lee, "Modeling and simulation of spacecraft power systems," *IEEE Trans. Aerosp. Electron. Syst.*, vol. 24, no. 3, pp. 295–304, May 1988.

[15] Z. Jiang, S. Liu, and R. A. Dougal, "Design and testing of spacecraft power systems using VTB," *IEEE Trans. Aerosp. Electron. Syst.*, vol. 39, no. 3, pp. 976–989, Jul. 2003.

[16] A. M. McNelis *et al.*, "Simulation and control lab development for power and energy management for NASA manned deep space missions," in *Proc. 12th Int. Energy Conv. Eng. Conf.*, 2014, Art. no. 3835.

[17] A. Myaing and V. Dinavahi, "FPGA-based real-time emulation of power electronic systems with detailed representation of device characteristics," *IEEE Trans. Ind. Electron.*, vol. 58, no. 1, pp. 358–368, Jan. 2011.

[18] N. Lin, S. Cao, and V. Dinavahi, "Comprehensive modeling of large photovoltaic systems for heterogeneous parallel transient simulation of integrated AC/DC grid," *IEEE Trans. Energy Convers.*, vol. 35, no. 2, pp. 917–927, Jun. 2020.

[19] G. N. Psarros, E. I. Batzelis, and S. A. Papathanassiou, "Partial shading analysis of multistring PV arrays and derivation of simplified MPP expressions," *IEEE Trans. Sustain. Energy*, vol. 6, no. 2, pp. 499–508, Apr. 2015.

[20] Q. Liu, T. Liang, and V. Dinavahi, "Real-time hierarchical neural network based fault detection and isolation for high-speed railway system under hybrid AC/DC grid," *IEEE Trans. Power Del.*, vol. 35, no. 6, pp. 2853–2864, Dec. 2020.

[21] B. Li, M. Y. Chow, Y. Tipsuwan, and J. C. Hung, "Neural-network-based motor rolling bearing fault diagnosis," *IEEE Trans. Ind. Electron.*, vol. 47, no. 5, pp. 1060–1069, Oct. 2000.

[22] T. Guillod, P. Papamanolis, and J. W. Kolar, "Artificial neural network (ANN) based fast and accurate inductor modeling and design," *IEEE Open J. Power Electron.*, vol. 1, pp. 284–299, Jul. 2020.

[23] V. Dinavahi and N. Lin, *Real-Time Electromagnetic Transient Simulation of AC-DC Networks*. Piscataway, NJ, USA: Wiley, 2021.

[24] E. B. Gietl, E. W. Gholdston, F. Cohen, B. A. Manners, and R. A. Delventhal, "The architecture of the electric power system of the international space station and its application as a platform for power technology development," in *Proc. 35st Intersociety Energy Conv. Eng. Conf.*, 2000, vol. 2, pp. 855–864.

[25] A. Jain and A. Kapoor, "Exact analytical solutions of the parameters of real solar cells using Lambert W-function," *Sol. Energy Mater. Sol. Cells*, vol. 81, pp. 269–277, 2003.

[26] "Silicon K6700B Wrapthru solar cells," May 2019. [Online]. Available: https://solarmuseum.org/cells/k6700b-wrapthru/

[27] T. W. Kerslake and D. A. Scheiman, "Off-nominal performance of the International Space Station solar array wings under orbital eclipse lighting scenarios," in *Proc. 3rd Int. Energy Convers. Eng. Conf.*, San Francisco, CA, USA, Aug. 2005, Paper E-15311.

[28] O. Tremblay and L.-A. Dessaint, "Experimental validation of a battery dynamic model for EV applications," *World Elect. Veh. J.*, vol. 3, no. 2, pp. 289–298, 2009.

[29] Lithium ion cells for satellites- power optimized," GS Yuasa, 2009. [Online]. Available: https://gsyuasa-lp.com/SpecSheets/GS_Yuasa_LSE_GEN_III_Power.pdf

[30] H. Wu, K. Sun, L. Zhu, and Y. Xing, "An interleaved half-bridge three-port converter with enhanced power transfer capability using three-leg rectifier for renewable energy applications," *IEEE J. Emerg. Sel. Top. Power Electron.*, vol. 4, no. 2, pp. 606–616, Jun. 2016.

[31] M. R. Patel, *Spacecraft Power Systems*. Boca Raton, FL, USA: CRC Press, 2005.

[32] S. De Simone, C. Adragna, C. Spini, and G. Gattavari, "Design-oriented steady-state analysis of LLC resonant converters based on FHA," in *Proc. Int. Symp. Power Electron., Elect. Drives, Automat. Motion*, 2006, pp. 200–207.

[33] "LLC Resonant Converter: Operation and design." Sep. 2012. [Online]. Available: https://www.infineon.com/dgdl/Application_Note_ResonantLLCConverterOperationandDesign_Infineon.pdf?fileId=db3a30433a047ba0013a4a60e3be64a1

[34] Infineon IHW30N135R5 resonant switching series IGBT module datasheet, 2019. [Online]. Available: https://www.infineon.com/dgdl/Infineon-IHW30N135R5-DataSheet-v02_03-EN.pdf?fileId=5546d462636cc8fb0163b0f490c430e4
[35] Microsemi ultrafast soft recovery rectifier diode APT2X101D120J, Mar. 2011. [Online]. Available: https://www.digikey.ca/en/products/detail/microchip-technology/APT2X101D120J/1494419
[36] S. Zhang, T. Liang, and V. Dinavahi, "Machine learning building blocks for real-time emulation of advanced transport power systems," *IEEE Open J. Power Electron.*, vol. 1, pp. 488–498, Nov. 2020.
[37] M. Mohri, A. Rostamizadeh, and A. Talwalkar, *Foundations of Machine Learning*. Cambridge, MA, USA: MIT Press, 2012, doi: 10.1109/TNNLS.2022.3151683.
[38] S. Skansi, *Introduction to Deep Learning: From Logical Calculus to Artifical Intelligence*. Berlin, Germany: Springer, 2018.
[39] S. Ruder, "Overview of gradient descent optimization algorithms," Sep. 2016, *arXiv:1609.04747*, doi: 10.1109/OJPEL.2020.3039117.
[40] D. P. Kingma and J. Ba, "Adam: A method for stochastic optimization," in *Proc. 3rd Int. Conf. Learn. Representations*, San Diego, CA, USA, 2015, pp. 1–15.
[41] Solar radiation and climate experiment (SORCE), 2020. [Online]. Availabe: https://lasp.colorado.edu/home/sorce/data/

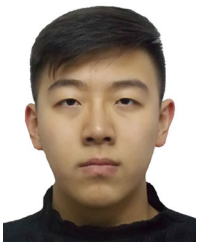

WEIRAN CHEN (Student Member, IEEE) received the B.Eng. degree in electrical engineering from Harbin Engineering University, Harbin, China, in 2018. He is currently working toward the Ph.D. degree in electrical and computer engineering with the University of Alberta, Edmonton, AB, Canada. His research interests include real-time simulation of power systems, power electronic systems, and field programmable gate arrays.

SONGYANG ZHANG (Student Member, IEEE) received the B.Eng. and M.Eng. degrees in electrical engineering from the Huazhong University of Science and Technology, Wuhan, China, in 2017 and 2019, respectively. He is currently working toward the Ph.D. degree in electrical and computer engineering with the University of Alberta, Edmonton, AB, Canada. His research interests include machine learning, real-time simulation, power electronics and field programmable gate arrays.

VENKATA DINAVAHI (Fellow, IEEE) received the B.Eng. degree in electrical engineering from the Visvesvaraya National Institute of Technology, Nagpur, India, in 1993, the M.Tech. degree in electrical engineering from the Indian Institute of Technology Kanpur, India, in 1996, and the Ph.D. degree in electrical and computer engineering from the University of Toronto, ON, Canada, in 2000. He is currently a Professor with the Department of Electrical and Computer Engineering, University of Alberta, Edmonton, AB, Canada. His research interests include real-time simulation of power systems and power electronic systems, electromagnetic transients, device-level modeling, large-scale systems, and parallel and distributed computing. He is a Fellow of the Engineering Institute of Canada.